EXPERIMENTAL INVESTIGATION OF SOLUBILITY TRAPPING IN 3D PRINTED MICROMODELS

Alexandros Patsoukis Dimou[1,4,5] (iD), Mahdi Mansouri Boroujeni[2] (iD), Sophie Roman[3] (iD), Hannah P. Menke[1] (iD), Julien Maes[1] (iD)

[1]Institute of Geoenergy and Engineering, Heriot-Watt University, Edinburgh, UK; [2]Laboratoire de Chimie Bactérienne, CNRS-Aix Marseille University UMR7283, Institut de Microbiologie de la Méditerranée, Marseille, France; [3]Institut des Sciences de la Terre d'Orléans, Univ. Orléans, CNRS, BRGM, ISTO UMR 7327, Orléans, France; [4]Institute of Fluid Science, Tohoku University, Aoba Ward, Sendai, Miyagi, Japan; [5]School of Physics and Astronomy, University of Edinburgh, Edinburgh, UK

1. VISUALIZATION CELL

In **Figure S1**, we present the transparent Perspex visualization cell in both its disassembled (**Fig. S1A**) and assembled (**Fig. S1B**) states. The cell consists of two main components: a container and a lid. The container features a cylindrical sample port with a diameter of 2.5 cm where the micromodel is positioned. A layer of polished 3D-printed transparent material is placed at the bottom of the port. The lid includes a piston of the same diameter to ensure a secure fit. Once the 3D-printed micromodel is placed inside the sample port, the lid is positioned on top of the container and secured with four screws to ensure proper sealing and prevent leakage. The bottom of the sample port and the 3D-printed layer contain two openings that allow for the connection of PEEK tubing, facilitating fluid injection and retrieval.

Figure S1: Schematic of the Perspex visualization cell used for the experiments.
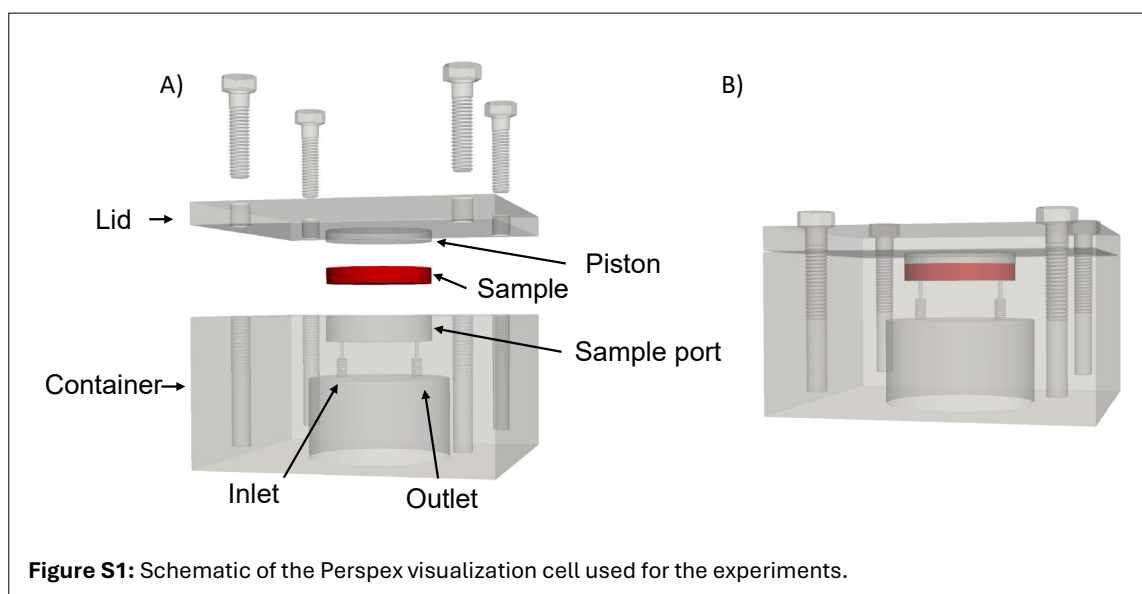
2. NUMERICAL METHODS

In the volume of fluid method, the location of the interface is given by the indicator function α, which is equal to the volume fraction of one phase in each grid cell. The density and viscosity of the fluid are given by volumetric averaging (**Eq. 1**, **Eq. 2**),

$$\rho = \rho_1 \alpha + \rho_2(1 - \alpha) \tag{1}$$

$$\mu = \mu_1 \alpha + \mu_2(1 - \alpha) \tag{2}$$

where ρ_i (kg.m^{-3}) and μ_i (Pa.s) are the density and viscosity of phase i. The velocity, pressure and species concentration in the domain are expressed in terms of single-field variables in a similar manner (**Eq. 3-5**),

$$\boldsymbol{u} = \boldsymbol{u}_1 \alpha + \boldsymbol{u}_2(1 - \alpha) \tag{3}$$

$$p = p_1 \alpha + p_2(1 - \alpha) \tag{4}$$

$$c = c_1 \alpha + c_2(1 - \alpha) \tag{5}$$

where u_i (m.s^{-1}), p_i (Pa) and c_i (kg.m^{-3}) are the velocity, pressure and species concentration in phase i. The phase advection equation is as follows (**Eq. 6**):

$$\frac{\partial \alpha}{\partial t} + \nabla \cdot (\alpha \boldsymbol{u}) + \nabla \cdot (\alpha(1 - \alpha) \, \boldsymbol{u}_r) = \frac{\dot{m}}{\rho_1} \tag{6}$$

where $\dot{m}$ (kg.m^{-3}.s^{-1}) is the mass transfer from phase 2 to phase 1 and $\boldsymbol{u}_r = \boldsymbol{u}_1 - \boldsymbol{u}_2$ is the relative velocity of the interface between the two phases (4). To limit numerical diffusion at the two-fluid interface, the relative velocity is modelled as a compressive velocity (**Eq. 7**),

$$u_r \equiv u_{comp} = \boldsymbol{n}_\Sigma \left[min \left(c_\alpha \frac{|\phi_f|}{A_f}, max \left(\frac{|\phi_f|}{A_f} \right) \right) \right] \tag{7}$$

where c_α is the compression constant (generally between 0 and 4), A_f is the area of face f and ϕ_f the volumetric flux across f. In all our simulations, c_α=1.0.

Assuming each phase is Newtonian and incompressible, and neglecting gravity effects as well as assuming the fluid properties are constant in each phase, the single-field momentum equation can be written as (2) (**Eq. 8**, **Eq. 9**):

$$\nabla \cdot \boldsymbol{u} = \dot{m} \left(\frac{1}{\rho_1} - \frac{1}{\rho_2} \right) \tag{8}$$

$$\frac{\partial \rho \boldsymbol{u}}{\partial t} + \nabla \cdot (\rho \boldsymbol{u}\boldsymbol{u}) = -\nabla p + \nabla \cdot \left(\mu(\nabla \boldsymbol{u} + \nabla \boldsymbol{u}^T) \right) + \boldsymbol{f}_{st} \tag{9}$$

where $\boldsymbol{f}_{st}$ (kg.m^{-2}.s^{-2}) is the surface tensions force, calculated using the Continuous Surface Force (CSF) method (1) (**Eq. 10**),

$$\boldsymbol{f}_{st} = \sigma \kappa \nabla \alpha. \tag{10}$$

σ (N.m^{-1}) is the interfacial tension, κ (m^{-1}) is the curvature at the interface which can be calculated as (**Eq. 11**) :

$$\kappa = -\nabla \cdot \boldsymbol{n}_\Sigma, \tag{11}$$

where n_Σ is the interface vector defined as (**Eq. 12**):

$$\boldsymbol{n}_\Sigma = \frac{\nabla \alpha}{\|\nabla \alpha\|}. \tag{12}$$

Assuming that the gas phase is pure and that the gas dissolves in the liquid phase with Henry's constant H and remains diluted, the single-field concentration equation satisfies the advection-diffusion equation given by the Continuous Species Transfer (CST) formulation (**Eq. 13**),

$$\frac{\partial c}{\partial t} + \nabla . \boldsymbol{F} + \nabla . \boldsymbol{J} = 0, \tag{13}$$

where $\boldsymbol{F}$ (kg.m^{-2}.s^{-1}) is the advective flux and J (kg.m^{-2}.s^{-1}) is the diffusive flux. Maes and Soulaine (3) showed that the advective flux can be written as (**Eq. 14**):

$$\boldsymbol{F} = c\boldsymbol{u} + \alpha(1 - \alpha)\frac{\nabla c \cdot \nabla \alpha}{\|\nabla \alpha\|^2}\boldsymbol{u}_r, \tag{14}$$

and the diffusive flux can be written as (3) (**Eq. 15**):

$$\boldsymbol{J} = -D^{SF}\nabla c + \boldsymbol{\Phi}, \tag{15}$$

where $\boldsymbol{\Phi}$ (kg.m^{-2}.s^{-1}) is the CST flux and D^{SF} (m^2.s^{-1}) is the single-field diffusion coefficient. The CST flux can be written as (**Eq. 16**):

$$\boldsymbol{\Phi} = (1 - \mathrm{H})D^{SF}\frac{c}{\alpha + H(1 - \alpha)}\nabla \alpha, \tag{16}$$

and the single-field diffusion coefficient can be expressed as (**Eq. 17**):

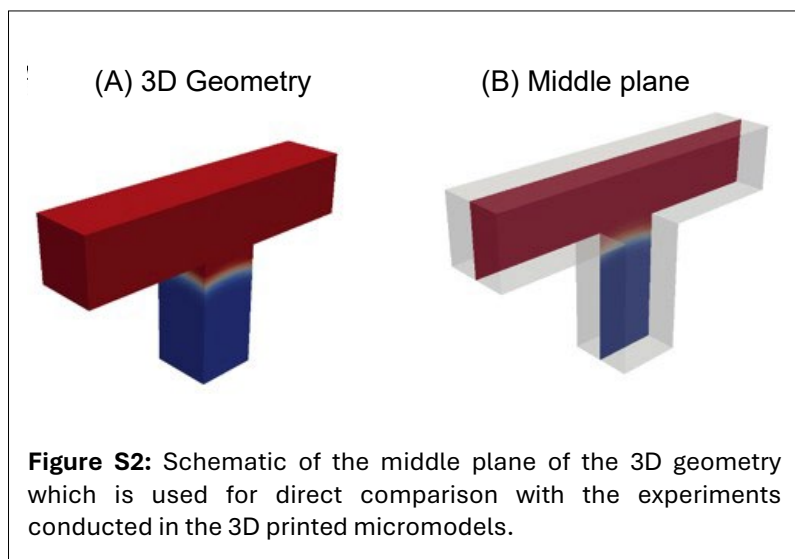$$D^{SF} = \frac{\alpha D_1 + H(1 - \alpha)D_2}{\alpha + H(1 - \alpha)}, \tag{17}$$

where D_i (m^2.s^{-1}) is the diffusion coefficient of phase i. Finally, the mass transfer $\dot{m}$ at the interface can be calculated as (**Eq. 18**):

$$\dot{m} = -\frac{D^{SF}\nabla c - \boldsymbol{\Phi}}{1 - \alpha} \cdot \nabla \alpha. \tag{18}$$

In **Figure S2B**, we present the 3D simulation geometry (**Fig. S1A**) alongside the middle slice of the same 3D geometry (**Fig. S1B**). The color scheme aids in differentiating between the phases: blue signifies the trapped CO_2 phase within the cavity, while red represents the water phase. To ensure an accurate comparison with the dissolution experiments conducted in the 3D printed micromodel devices, we specifically measure the fraction of CO_2 trapped in the cavity at the middle slice.
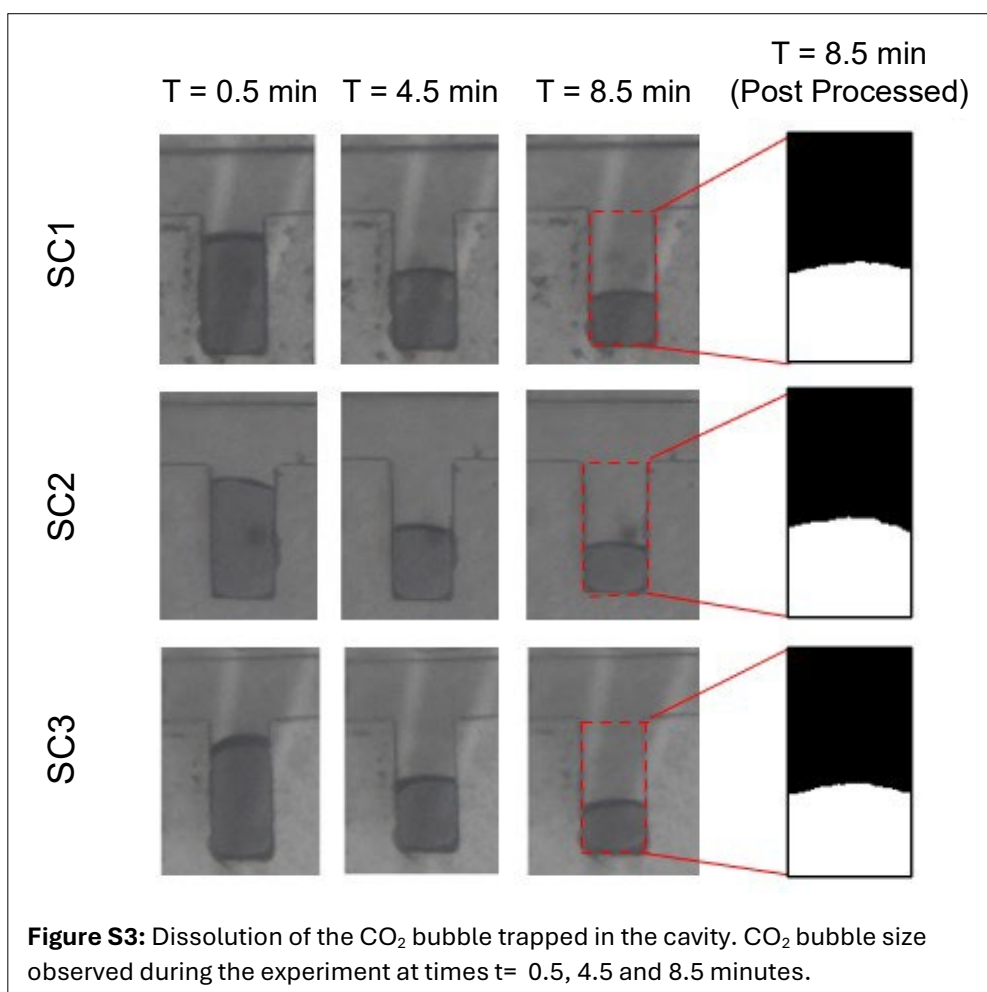
3. EXPERIMENTAL RESULTS

In **Figure S3**, we present the experimental results obtained from the dissolution experiments conducted in the Single Cavity (SC) geometry. At a specific time, (T = 0.5 min), the water has completely passed the cavity, leaving behind only the trapped CO_2 (represented by dark grey shading) within the geometry. In **Figure S3** it is demonstrated that the amount of CO_2 present in the cavity is visually the same across three identical geometries (SC1, SC2, and SC3) at various time intervals (T = 0.5, 4.5, and 8.5 min). This agreement in CO_2

Figure S2: Schematic of the middle plane of the 3D geometry which is used for direct comparison with the experiments conducted in the 3D printed micromodels.

quantity indicates the reliability of our measurements and shows the repeatability of the dissolution experiments in the 3D printed micromodels.

Moreover, in **Figure S3**, we highlight the specific area of the cavity where the measurements are conducted, marked in red. Additionally, we provide the post-processed image of this area which is used pixel calculation for accurately determining the amount of CO_2 inside the cavity (white region).

In **Figure S4**, we present the experimental results obtained from the dissolution experiments conducted in the Triple Cavity (TC) geometry. At a specific time point (T = 1 min), it is evident that the water has passed through all three cavities, leaving behind only the trapped CO_2 (represented by dark grey shading) within the geometry.

Figure S3: Dissolution of the CO_2 bubble trapped in the cavity. CO_2 bubble size observed during the experiment at times t= 0.5, 4.5 and 8.5 minutes.

Furthermore, in **Figure S4**, we observe that the amount of CO_2 present in the cavity is consistent across three identical geometries (TC1, TC2, and TC3) at various time intervals (1, 5, and 9 min). This agreement in CO_2 quantity among the cavities reinforces the reliability of our measurements and experimental setup.

Figure S4: CO_2 bubble sizes observed during the experiment at the three identical TC geometries at times T = 1, 5 and 9 min.
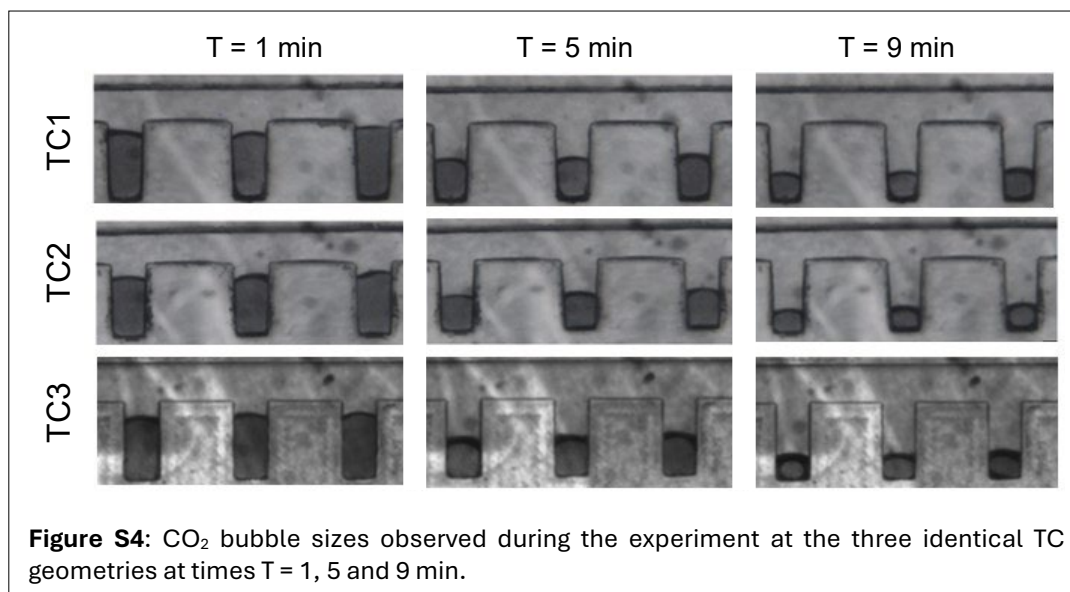
Since gravity is perpendicular to the cavity, the trapped CO_2 bubble, initially, remains restricted in its movement (**Fig. S5A**). As the bubble gradually dissolves, it eventually reaches the bottom of the cavity (**Fig. S5B**). Given that CO_2 is less dense than water, there comes a point when the bubble detaches from the lower wall and rises to the upper wall due to buoyancy forces (**Fig. S5C**). Because our recordings capture the planar axis, this detachment is observed as an increase in the apparent surface area of the CO_2 bubble.

Figure S5: The impact of gravity to the bubble position.
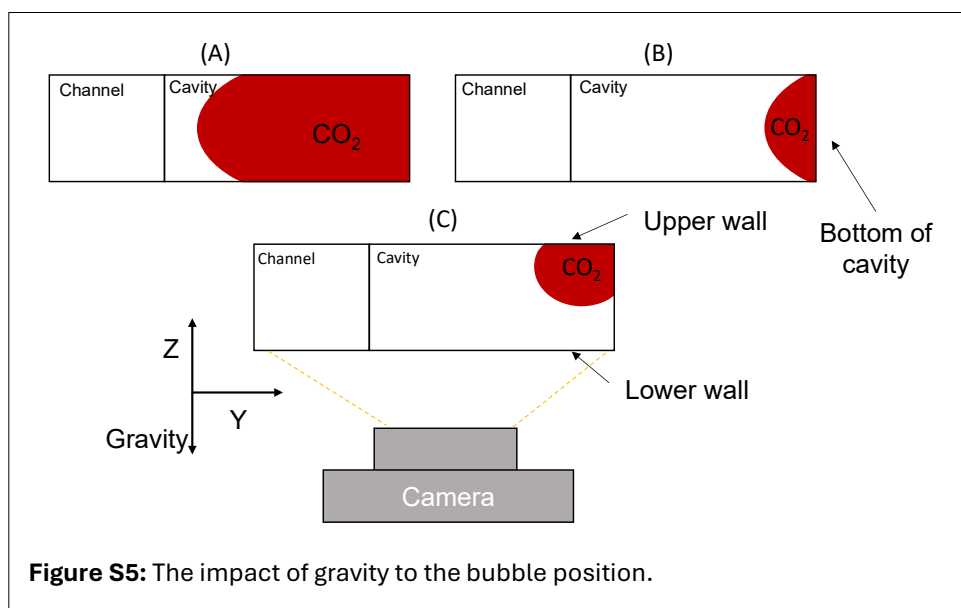
REFERENCES

1. Brackbill, J. U., Kothe, D. B., & Zemach, C. (1992). A continuum method for modeling surface tension. *Journal of Computational Physics*, 100(2), 335–354. https://doi.org/10.1016/0021-9991(92)90240-Y
2. Hirt, C. W., & Nichols, B. D. (1981). Volume of fluid (VOF) method for the dynamics of free boundaries. *Journal of Computational Physics*, 39(1), 201–225. https://doi.org/10.1016/0021-9991(81)90145-5
3. Maes, J., & Soulaine, C. (2020). A unified single-field Volume-of-Fluid-based formulation for multi-component interfacial transfer with local volume changes. *Journal of Computational Physics*, 402, 109024. https://doi.org/10.1016/j.jcp.2019.109024
4. Rusche, H. (2003). *Computational fluid dynamics of dispersed two-phase flows at high phase fractions*. (PhD Thesis). Imperial College London http://hdl.handle.net/10044/1/8110